Atmos. Meas. Tech. Discuss., doi:10.5194/amt-2015-409, 2016
Manuscript under review for journal Atmos. Meas. Tech.
Published: 1 February 2016

Atmospheric Measurement Techniques Discussions
Open Access

Top-of-the-atmosphere shortwave flux estimation from UV satellite observations: An empirical approach using data from the A-train constellation

Pawan Gupta[1, 2], Joanna Joiner[2], Alexander Vasilkov[3, 2], P. K. Bhartia[2]

[1] {Universities Space Research Association, Greenbelt, MD}
[2] {NASA Goddard Space Flight Center, Greenbelt, MD}
[3] {Science Systems and Applications, Inc., Greenbelt, MD}

Correspondence to: Pawan Gupta (pawan.gupta@nasa.gov)

Abstract

Estimates of top of the atmosphere (TOA) radiative flux are essential for the understanding of Earth's energy budget and climate system. Clouds, aerosols, water vapor, and ozone (O_3) are among the most important atmospheric agents impacting the Earth's short-wave (SW) radiation budget. There are several sensors in orbit that provide independent information related to these parameters. Having coincident information from these sensors is important for understanding their potential contributions. The A-train constellation of satellites provides a unique opportunity to analyze near-simultaneous data from several of these sensors. In this paper, retrievals of cloud/aerosols parameters and total column ozone (TCO) from the Aura Ozone Monitoring Instrument (OMI) have been collocated with the Aqua Clouds and Earth's Radiant Energy System (CERES) estimates of TOA SW flux (SWF). We use these data to develop a variety of neural networks that estimate TOA SWF globally over ocean and land using only OMI data as inputs. OMI-estimated TOA SWF reproduces the independent CERES data with high fidelity. The global mean daily TOA SWF calculated from OMI is consistently within ±1% of CERES throughout the year 2007. Application of our neural network to other ultraviolet sensors, both past and future, may provide unique estimates of TOA SWF. For example, the well-calibrated Total Ozone Mapping Spectrometer (TOMS) series could provide estimates of TOA SWF dating back to late 1978.

Atmos. Meas. Tech. Discuss., doi:10.5194/amt-2015-409, 2016
Manuscript under review for journal Atmos. Meas. Tech.
Published: 1 February 2016

1 Introduction

The Earth's energy budget constrains the general circulation of the atmosphere and determines the climate of the Earth-Atmosphere system; it is therefore also an indicator of possible climate changes (Hatzianastassiou, et al., 2004). There is a long history of attempts to estimate Earth's albedo and energy budget (Dines, 1917; Hartmann et al., 1986). With the advent of the satellite remote sensing era, it became possible to directly measure the albedo of the Earth. Subsequently, the shortwave energy balance at the TOA and the role of clouds, aerosols, and trace gases has been studied using satellite measurements (Ramanathan et al., 1989; Yu et al., 2006; Bellouin et al., 2005; Loeb et al., 2005; Patadia et al., 2008; Joiner et al., 2009).

The Earth Radiation Budget Experiment (ERBE) was launched in October 1984 by the space shuttle Challenger and provided long- and short-wave (SW) radiation parameter measurements. Top-of-atmosphere short-wave (TOA SW) radiative parameter estimates from ERBE (Barkstrom, 1984), Barkstrom and Smith (1986) showed that clouds approximately double the albedo of Earth from an estimated clear-sky value of 0.15 to its average all-sky value of 0.3 (Ramanathan et al., 1989; Harrison et al., 1990). The next generation of broadband instruments, the Cloud and the Earth's Radiant Energy System (CERES), draws heavily on ERBE heritage. Since its first launch in 1997 onboard the NASA Tropical Rainfall Measurement Mission (TRMM), CERES has provided continuous observations that can be used to understand the role of clouds and the energy cycle in global climate change (Wielicki et al., 1995; Loeb et al., 2012).

Continuous and coincident measurements of radiative fluxes and atmospheric components facilitate research studies to estimate and understand the role of different atmospheric components on the planetary energy balance. Although CERES provides state-of-art estimates of TOA radiative fluxes, it does not make measurements of individual atmospheric components that impact those fluxes. Several studies have utilized aerosol and cloud information from high spatial resolution MODerate resolution Imaging Spectroradiometer (MODIS) measurements to quantify their impact on TOA fluxes (Yu et al., 2006; Patadia et al., 2008; Zhang et al., 2005b; Loeb et al., 2005; Oreopoulos et al., 2009). Several attempts have also been made to convert narrowband radiances into broadband fluxes using regression or more sophisticated statistical approaches (Chevallier et al., 1998; Hu et al., 2002; Domenech and Wehr 2011; Vázquez-Navarro et al., 2012).

Atmos. Meas. Tech. Discuss., doi:10.5194/amt-2015-409, 2016
Manuscript under review for journal Atmos. Meas. Tech.
Published: 1 February 2016

Atmospheric Measurement Techniques Discussions

The Ozone Monitoring Instrument (OMI), flying on NASA's Aura satellite since 2004, provides information about components important for the Earth's SW radiation budget including the effective cloud/aerosol fraction (Stammes et al., 2008; Joiner and Vasilkov, 2006) and total column ozone (TCO) (Veefkind et al., 2006; McPeters et al., 2008; Kroon et al., 2008). OMI-retrieved parameters can be utilized to understand their role in the Earth's SW energy budget.

To model the spatial and temporal distribution of the TOA short-wave flux (SWF) requires a description of the components that control the transfer of solar radiation within the Earth-Atmosphere system. When required parameters are missing or incomplete, a statistical approach is an alternative for estimation of TOA SWF. Here, we develop an artificial neural network (NN) model to estimate TOA SWF. Artificial neural networks are algorithms that simulate biological neural networks by learning and pattern recognition (Bishop, 1995). NNs have been used by many scientific disciplines, including Earth science, to identify patterns and extract trends in imprecise and complicated non-linear data (e.g., Lee et al., 1990; Gupta and Christopher, 2009). In radiation studies, NNs have been used to estimate TOA and surface short-wave fluxes based on radiative transfer calculations with or without data from satellites (e.g., Krasnopolsky et al., 2008, 2010; Takenaka et al., 2011; Vázquez-Navarro et al., 2012; Jiang et al., 2014). CERES TOA flux algorithms have also used NNs to generate Angular Distribution Models (ADMs) in the absence of sufficient high-resolution imager information for reliable scene identification (Loukachine and Loeb, 2003; 2004).

In this study, we utilize OMI cloud, and ozone products along with other ancillary data to estimate TOA SWF. We develop NNs that take OMI-derived quantities as inputs and provide CERES-equivalent TOA SWF as the output. The trained NN models are optimized to run with data sets from OMI or similar sensors and can be applied generally to different seasons and years. For example, the neural network-based models we develop here can be applied to similar measurements from the Total Ozone Mapping Spectrometer (TOMS) instruments. The main objective of this study is to assess how well TOA SWF can be estimated using OMI cloud and ozone products with NNs when CERES data are used for training. The developed NNs can then be applied to other instruments with similar accuracy.

The paper is organized as follows: Section 2 describes the various satellite data sets utilized in the study. Section 3 discusses the development of NN models including the selection of input

Atmos. Meas. Tech. Discuss., doi:10.5194/amt-2015-409, 2016
Manuscript under review for journal Atmos. Meas. Tech.
Published: 1 February 2016

parameters. Section 4 evaluates our NN estimation of TOA SWF using independent CERES data over ocean and land. Section 5 summarizes the results and discusses future work.

2 Satellite Data Sets and Coincident Sampling

Under clear-sky conditions, TOA SWF is affected by the Earth's surface properties, atmospheric absorbers such as water vapor, ozone, and aerosols, and scattering by air molecules and aerosols particles. Over ocean, surface properties can be characterized by ocean color and roughness of the ocean surface. Under cloudy sky conditions, cloud optical properties such as the cloud optical thickness, geometrical cloud fraction, effective radius, and phase function affect TOA SWF. In clear and cloudy skies, the solar zenith angle (SZA) and Sun-Earth distance (SED) impact the TOA SWF.

In this work, we make use of data sets mainly from two passive sensors in A-train constellation of satellites that fly within 15 minutes of each other: 1) Aura OMI with an equatorial crossing time of ~13:45 ± 15 minutes local time and 2) Aqua CERES with an equatorial crossing time of ~13:30 local time. We primarily use 2007 data over global oceans for the training, testing, and validation of neural network models. Starting around 2008, OMI experienced an anomaly presumably due to material outside the sensor that adversely affects the quality of the level 1B and level 2 data products in a portion of its 60 rows across the swath. Our study focuses on data in 2007 that are not significantly affected by these anomalies.

2.1.1 CERES

The first CERES instrument flew on the TRMM satellite, launched in November 1997, and provided data until 2000. Five CERES instruments are currently operating; two on NASA's Terra satellite (FM1 and FM2), two on NASA's Aqua satellite (FM3 and FM4), and one on the Suomi National Polar-orbiting Partnership (NPP) satellite (FM5). These CERES instruments provide radiometric measurements of the Earth's atmosphere from three broadband channels: 1) A shortwave channel to measure reflected sun light (0.3-5 μm), 2) a long wave channel to measure Earth-emitted thermal radiation in the window region (8-12 μm), and 3) a total channel to measure radiation from 0.3 to 200 μm.

CERES radiances are converted to TOA fluxes using angular dependent models (ADMs). The CERES science team has an extensive database of ADM's for clear- and cloudy-sky over both land and ocean (Loeb et al., 2005). The ADMs heavily depend upon the observed scene type and are sensitive to surface characteristics as well as cloud and aerosol optical properties (Loeb et al., 2003; Zhang et al., 2005a; Patadia et al., 2011). The ADMs over ocean are dependent upon wind speed and aerosol optical thickness along with sun-satellite geometry (Zhang et al., 2005a).

The Aqua spacecraft carries two identical CERES instruments: one operates in a cross-track scan mode (FM3) and the other in a biaxial scan mode (FM4). Measurements from the biaxial scan mode were used to develop the ADMs; this provided considerable improvement over the previous generation of instruments including the ERBE (Loeb et al., 2003; 2007).

This study uses the Single Scanner Footprint (SSF, Edition 3A) TOA SWF obtained from the Aqua CERES FM3. The SSF product is a merge of CERES parameters with coincident cloud and aerosol parameters derived from the Aqua MODIS (Loeb et al., 2003). The high-resolution (1x1 km^2 at nadir) MODIS imager data are used to characterize the clear and cloudy portions of the larger CERES pixel (20x20 km^2 at nadir).

2.2 OMI

OMI provides hyper-spectral measurements of Earth-backscattered sunlight from UV to visible wavelengths (~270-500 nm) with a spectral resolution of the order of 0.5 nm (Levelt et al., 2006). Its spatial resolution is 13x24 km^2 at nadir with a swath width of about 2600 km. Cloud, aerosol, and total column ozone (TCO) products from OMI are used in this study. Specifically, the cloud-aerosol Optical Centroid Pressure (OCP), effective cloud fraction (f_c), Lambertian-Equivalent Reflectivity (LER) at 354.1 nm, Solar Zenith Angle (SZA), Relative Azimuth Angle (RAA), and Viewing Zenith Angle (VZA) are obtained from the OMI cloud products as detailed below, and Aerosol Index (AI) and TCO are obtained from the OMI-TOMS total ozone product (OMTO3, version 8.5, collection 3) (McPeters et al., 2008).

Cloud-aerosol OCP, also known as effective cloud pressure, is a measure of the reflectance-weighted pressure reached by incoming solar photons (Joiner et al., 2012). It is distinct from the cloud-top pressure (CTP). While CTP is the more important parameter needed for TOA long-wave flux, OCP is more related to atmospheric absorption in the short-wave. OCP is derived from OMI observations using two different methods (Stammes et al., 2008): 1) filling-in of solar Fraunhofer lines from rotational-Raman (RR) scattering in the UV (the OMCLDRR product) (Joiner and Bhartia, 1995; Joiner et al., 2004) and 2) collision-induced oxygen absorption (O_2-O_2) at 477 nm (the OMCLDO2 product) (Stammes et al., 2008;

Atmos. Meas. Tech. Discuss., doi:10.5194/amt-2015-409, 2016
Manuscript under review for journal Atmos. Meas. Tech.
Published: 1 February 2016

Atmospheric Measurement Techniques Discussions

Acarreta et al., 2004). Unless otherwise specified, we use the f_c and OCP from OMCLDRR product here.

OMI cloud and trace-gas algorithms use a simplified mixed Lambertian cloud model to estimate observed radiances I_m. In this scenario, a pixel is modeled as a having components from clear and cloudy sub-pixel weighted using an effective cloud fraction f_c, i.e.,

$$I_m = I_g\,(1 - f_c) + I_c f_c \tag{1}$$

where I_g and I_c are the radiances computed in the Rayleigh atmosphere for Lambertian surfaces corresponding to the clear and cloudy portions of the scene, respectively; f_c is defined as the fraction of the Lambertian cloud covering the pixel and is related to both the geometric cloud fraction and cloud optical thickness. It contains information similar to the Lambertian-equivalent reflectivity of the scene (related to cloud and surface reflectivities). However, because it attempts to account for variations in the Earth's surface reflectivity, it is a more spectrally invariant quantity and therefore potentially more highly correlated with TOA SWF.

Formally, the effective cloud fraction is wavelength-dependent because it is defined by spectral quantities (Stammes et al., 2008). We conducted a simulation experiment to evaluate the wavelength dependence of f_c. In this experiment, we simulate observed TOA radiances as a weighted sum of the clear-sky and cloudy radiances, i.e.,

$$I_m = I_g\left(1 - f_g\right) + I_c \times f_g \tag{2}$$

where I_c is the cloudy radiance computed with a plane-parallel cloud model that depends on cloud optical thickness, and f_g is the geometrical cloud fraction. In our simulation, clouds have a vertically uniform distribution of the extinction coefficient and phase function. We use a cloud top height of 5 km and a cloud layer thickness of 1 km. The assumed cloud optical depth of 20 is spectrally-independent within the 320-1400 nm wavelength range. The spectrally-independent optical thickness is a good approximation for clouds with sufficiently large particles (Deirmendjian, 1969). We neglect gaseous absorption in the specified spectral range. Three models of cloud phase function are used: 1) ice crystals with an effective diameter of 60 µm (Baum et al., 2014), 2) C1 water droplets with an effective diameter of 12 µm (Deirmendjian, 1969), and 3) the Heneye-Greenstein (HG) model (e.g. van de Hulst and Irvine, 1963) with an asymmetry parameter of 0.85. We use a simplified model of the spectral ground reflectance: R_g = 0.05 at λ<700 µm, R_g = 0.2 at λ>700 µm. We then calculate f_c by inverting Eq. 1 assuming a Lambertian cloud with a reflectivity of 0.8; this is commonly used for trace-gas algorithms (Stammes et al., 2008).

Figure 1 shows the spectral dependence of f_c calculated for f_g =0.5, SZA = 45^0, and at nadir for the three phase functions assuming a cloud single scattering albedo of unity. It can be seen that f_c is nearly invariant with wavelength over a wide spectral range; it changes by only a few percent even for the steep change in the ground reflectance (simulating the so-called red-edge) at 700 nm. This result holds when other input parameters in our simulation are varied. The near spectral invariance of f_c suggests that it will be highly correlated with TOA SWF and thus a good predictor in a statistical model of TOA SWF.

We have used the following modified cloud fraction parameter, f_{c_mod}, as a predictor to estimate TOA short wave flux:

$$f_{c\_mod} = f_c \times \cos(SZA) \times \left(1/_{SED^2} \right)$$

where SED is the sun-Earth distance. The modification accounts for variation in the incoming solar irradiance. If SED is excluded from the input parameters, this creates time-dependent biases in the estimated TOA SWF. Figure 2 demonstrates that the relationship between TOA SWF and f_{c_mod} is highly linear and that this single parameter captures much of the variability in TOA SWF.

2.3 Ancillary Data

In addition to OMI data, a SeaWiFs-derived chlorophyll concentration (Chl) climatology is used as an input predictor when f_c < 1. The Precipitable Water (PW) and 2 m surface wind speed (Wind) are also used as predictors; these are provided in the CERES SSF data set and are taken from the GEOS 4 reanalysis (Bloom et al., 2005).

2.4 Coincident Sampling of OMI and CERES

Because the sizes of the OMI (13 km x 24 km) and CERES (20 km^2) pixels are similar at nadir, we perform a simple spatial collocation by finding the closest CERES pixel corresponding to each OMI pixel. OMI and CERES collocated pixels are only included in our training and validation samples when the distance between centers of OMI and CERES pixels is less than 20 km. We examine the frequency distribution of the distance between OMI and CERES pixels of all the collocated data sets and found that most of the collocated data (98% and 60%) have distances less than 20km and 10km, respectively. We do not include pixels with viewing zenith angles > 60^o. At these angles, OMI and CERES pixels become significantly larger (~150 km for OMI and ~200 km for CERES in the cross track direction) and may contain different scene types. We also mask OMI pixels with AI > 1 to avoid heavy absorbing aerosol loaded scenes where the f_c and OCP are known to contain errors (Vasilkov et al., 2008). The quality-controlled collocated data are averaged on equal latitude and longitude grids of 1^o x 1^o for training, testing, and validation of the neural networks.

Although the NN training includes data from CERES and other ancillary data sets but the trained NN provides TOA SWF similar to CERES using predominantly retrievals from OMI measurements. Therefore, the NN produced TOA SWF flux will be referred as OMI estimated SWF throughout the manuscript.

3 Artificial Neural Network Model

3.1 General NN architecture and training approach

The general neural network architecture has three layers of neurons: an input layer, a hidden layer, and an output layer with standard multi-layer network architecture. We use the same number of neurons in the hidden layer as in the input layer as this produced generally good result. The input layer has an identity activation function; all other layers are connected by a sigmoid activation functions (Equation 3).

$$y(x) = \frac{1}{1+e^{-x}} \tag{3}$$

The network normalizes both input and output data sets with a unique linear mapping for each input and output parameter. Figure 3 provides an example of a schematic of the network used in our study. Here we used two different NN models: one with nine nodes or parameters (NNM1) and a second with seven nodes (NNM2) in the input layer. Both of these models have one node (TOA SWF) in the output layer. Figure 3 also lists the input parameters corresponding to the NNM1 and NNM2 models. The NNM1 model is optimized for ocean cases where the OMI f_c < 1.0, whereas NNM2 is optimized for cases where f_c = 1 (saturated cases).

Neural network-based models require optimized training to produce accurate outputs. Here we use a standard back propagation training algorithm (Hertz et al., 1991), where inputs are iteratively sent to the neural network. In back propagation, the hidden layer weights associated with each input parameter are modified through the training process that minimizes errors between the targets and outputs (Bishop, 1995; Gardner and Dorling, 1998). After each iteration, the error is propagated backward through the network and weights are modified to bring the actual response of the network closer to the desired output in a statistical sense. The function minimized during the training is a sum of squared errors of each output for each training pattern. Once the network is trained, it can be evaluated using independent data (i.e., not used in the training data set).

3.2 Impact of different input parameters

Here we examine the impact of using various input parameters on the derived neural networks. This exercise is performed using data with $f_c < 1$ with one month of the data over ocean (January 2007). Table 1 presents the performance of eight different NNMs, denoted models a through h, with various input parameters listed in Table 1 and described in more detail in sections 3.2.1-3.2.2.

3.2.1 Inclusion of OMI UV-derived parameters

In model a, we have combined the effects of SZA, SED and f_c into a single input parameter called f_{c_mod}, which is defined in the section 2.2. Use of this modified input parameter alone explains about 94% (R=0.97) of the variability in TOA SWF. As we add other parameters in models b to h, we observe small improvements in the OMI-estimated TOA SWF. Figure 4 shows the spatial distribution of monthly mean OMI-CERES SWF differences for these models.

The TOA SWF is estimated from a measured radiance and therefore the observational geometry factors in. The addition of satellite viewing geometry parameters (VZA, RAA) to model a provides improvements in areas of high biases and reduces the standard deviation from 37.1 Wm^{-2} to 31.4 Wm^{-2}. Model c tests the ability of 354 nm reflectivity (LER) to predict TOA SWF in place of f_{c_mod}. Although the statistical parameters in table 1 corresponding to models b and c are very similar, we note spatial differences in the OMI-CERES TOA SWF in Figure 4. Further analysis reveals that the f_c-based model b provides more accurate flux estimation as compared with the LER-based model for a larger range of fluxes.

The inclusion of TCO (model d) as an input parameter positively impacts TOA SWF estimation as shown in Figure 4 (d); the high positive biases in the tropical Pacific and Indian

Atmos. Meas. Tech. Discuss., doi:10.5194/amt-2015-409, 2016
Manuscript under review for journal Atmos. Meas. Tech.
Published: 1 February 2016

oceans and in the region near 60^{o}N have been reduced. The percentage of monthly mean OMI-CERES data that falls within ±8% increases from 91% in model c to 94% in model d.

Model e adds cloud OCP to the input parameters included in model b. OCP also improves SWF estimates; the regions where improvement occurs are different from those improved by using TCO. Model f shows that when TCO and OCP are used together as input parameters, there is further improvement in SWF estimation. Although the global statistics in table 1 do not clearly reflect this improvement, Figure 4(f) shows that inclusion of OCP and O3 reduces biases in many regions, most prominently in the tropics. The percentage of total OMI samples (monthly mean) within ±8% of CERES increases from 92% in model b to 95% in model f. Apart from these parameters, we also evaluated the inclusion of AI as an input parameter (not shown here). We found that overall it does not significantly improve the results; however it does provide some improvement in regions with high AI values.

3.2.2 Addition of meteorological and other ancillary data

The impact of surface winds and total column water vapor (model g in Figure 4g) is more prominent in the tropics than in other regions. Inclusion of chlorophyll and LERs in model h removes some of the notable low biases in TOA SWF near the coast of Northern China, Caspian Sea, and Black Sea. Furthermore, model h corrects for negative biases in areas with high TOA SWFs, most likely due to the inclusion of LER. The model h produces 89% (99%) of OMI-estimated monthly mean TOA SWFs within ±5% (±12%) of CERES and is best of the eight models.

3.3 Consistency over time

We next examine the performance of the NN model h with respect to different input samples. Figure 5(a-b) presents the results from two different years over ocean. We first examine the robustness of the NN for detection of inter-annual variability. In this exercise, we trained with data from the first 15 days of January 2007 as above, and applied it to data from the entire months of January 2007 (Figure 5a) and January 2006 (Figure 5b). Figure 5a and b shows that the NN performance is consistent between years. Although the number of samples in January of 2006 and 2007 is a bit different, the NN model produces similar statistics. The color of each coincident pair (10x10 Wm^{-2} intervals) represents the density (%) of the matchup. The solid black 1 to 1 line is shown with three dotted lines on both sides that represent envelopes of ±5%, ±10%, and ±15% OMI-CERES differences.

Atmos. Meas. Tech. Discuss., doi:10.5194/amt-2015-409, 2016
Manuscript under review for journal Atmos. Meas. Tech.
Published: 1 February 2016

In the next test, we applied the same model (trained on January 2007) to July 2007. In this case, results were degraded as compared with application to January data. We then trained the same network (with the same input parameters) using a subset of data from July 2007 and applied it to the entire month of July 2007. Results were similar to those of training and application to January. This exercise suggests that we may need to use different models for different months or expand our training data set for application to different months.

We next use data from the 1st day of each month of 2007 for training and data from the 16th day of each month of 2007 for evaluation and gridded the data at 1^{o} latitude by 1^{o} longitude resolution. The comparisons with CERES using the training and validation data are consistent as shown in Figure 6. The mean bias in both training and validation data sets is close to zero whereas standard deviation remains stable and close to 30 Wm^{-2} in two independent model runs. The almost identical values of statistical parameters for training and validation data demonstrate that the neural network has been well trained. For example, there is a high degree of linear correlation (R = 0.98 or R^2 =0.96) and slopes close to 1 (0.96) in both training and validation comparisons. Further analysis shows that 83%, 70% and 43% of TOA SWF estimated from OMI (training and validation data combine) lie within the 15%, 10%, and 5% of the CERES TOA SWF, respectively. The global standard deviation of the daily OMI-CERES is about 30 Wm^{-2}.

Further evaluation of the entire year reveals that this NN is appropriate for all months. Therefore this model will be used for subsequent analysis in this study. Creating more networks as a function of scene type or for different latitude belts or even for different months/seasons will improve results in certain regions. However, based on our results, we simplified the approach by minimizing the number of networks.

3.4 Case of f_c =1

About 1-2 % of total coincident data correspond to f_c = 1, typical of overcast conditions with optically thick clouds. These cases were modeled using a simpler neural network model with inputs of LER, SZA, VZA, RAA, OCP, O3, and PW, the surface-related parameters (surface wind speed and chlorophyll content) do not produce a significant impact for ECF=1 and have therefore been removed. Subsequent results use combined output from the two separate models for f_c <1 and f_c =1.

4 Results and Discussion

4.1 Bias and RMSE as a function of effective cloud fraction

Figure 7 presents the Root Mean Square Error (RMSE), RMSE Normalized by CERES flux (NRMSE in %), data sample (%), and bias (%) for 5% ECF bins. This analysis includes both training and validation data as presented in Figure 6. The RMSE varies between about 24-35 Wm^{-2} and continuously increases with cloud fraction (and observed flux). The NRMSE, on the other hand, continuously decreases with ECF from about 18% for 5% ECF to ~6% for overcast conditions. The bias represents the mean error (in %) for each ECF bin. The mean global bias shows more variability than RMSE and is highest (2.9%) for about 10% ECF. The bias decreases sharply from 2.9% at f_c =0.1 to about 1.2% at f_c =0.4. The bias remains low (<1.2%) for f_c > 0.4 (usually associated with frontal or deep convective clouds). The higher biases for lower f_c (usually associated with thin cirrus and broken clouds) are likely related to higher noise and uncertainties in OMI cloud parameters. For example, (Joiner et al., 2012) showed that cloud OCP errors increase with decreasing f_c. The biases may also be related to absorbing aerosol in the scene, particularly when it overlies clouds. This will be illustrated in more detail below as we show spatial variations in OMI-CERES differences.

4.2 Effects of Spatial and Temporal Averaging

In order to evaluate the NN performance at different spatial and temporal scales similar to those used by the climate community, we use data from July 2007. Figure 8 presents a comparison of daily CERES and OMI TOA SWF over ocean for 6 spatial scales: the OMI native pixel (13x24 km^2 at nadir) and 0.5°, 1°, 2°, 5°, and 10° gridded spatial resolutions. Statistical parameters for these comparisons are reported in Table 2. As expected, the pixel level data are much noisier than the gridded data owing to collocation noise in partly cloudy cases, but the slope (0.96) is still close to 1, and the linear correlation coefficient is 0.96 with a standard deviation of 47.7 Wm^{-2}. Below 300 Wm^{-2}, where the sample density is highest, the NN slightly underestimates the CERES SWF. The mean bias of the OMI-estimated SWF with respect to CERES is -1.4 Wm^{-2}. This bias may be due to a combination of effects including uncertainties in the input parameters as well as the limitations of the NN model itself. For example, we have excluded pixels with a clear signature of absorbing aerosols (OMI derived UV aerosol index > 1) where OMI effective cloud fractions and pressures may be in error in both the training and validation data. However, in some regions where smoke and dust overlaying clouds is common (e.g., west coast of Africa), pixels with erroneous cloud fractions owing to small amounts of absorbing aerosol may be present in both the training and validation data. This may produce errors in the NN model and will be examined in more detail below.

For the daily data, as the spatial averaging scales increase from 0.5° to 10°, the OMI-estimated SWF becomes almost identical to CERES; the correlation coefficient increases from 0.97 to 0.99, and the slope increases from 0.96 to 0.97. The percentage of OMI data that falls within ±5% of CERES increases from 37% for 0.5° to 69% for 10° grids. About 87% percent of OMI-estimated 2° gridded daily mean TOA SWFs are within 15% of CERES data.

Figure 9(a-d) shows 2D histograms of monthly mean gridded data over ocean at 0.5°, 1°, 2°, and 5° spatial resolutions, respectively. The monthly inter-comparisons of OMI and CERES SWF show excellent agreement at all spatial resolutions with correlation coefficients of 0.99 and slopes of 0.98 (Table 2). The global mean biases vary between -1.8 and 0.25 Wm^{-2}. The standard deviations vary between 6.6 and 12.9 Wm^{-2} for the different spatial resolutions. Ninety seven percent of monthly mean 1° OMI estimated TOA SWFs are within 15% of those derived from CERES, and 93% are within 10%.

4.3 Spatial Distribution of TOA SWFs over ocean

Figure 10 presents the spatial distribution of 1° monthly mean (July 2007) TOA SWF from CERES (Fig. 10a) and the difference with the OMI in Wm^{-2} (Fig. 10b) and percent difference (Fig. 10c). There are subtle differences between the NN and CERES estimates of TOA SWF as shown in Figure 10b and c. The OMI-CERES histograms (Fig. 10d) show that for 44% (79%) samples, NN fluxes are within ±2 (±5) % of CERES fluxes. About 9% of the samples have biases of ±8% or more. Overall, the northern hemisphere shows better agreement than southern hemisphere during July (boreal summer). This could be due to larger errors in the OMI cloud products at higher solar zenith angles. The low biases on the west coast of Africa may be due to the presence of absorbing aerosols, particularly when they occur over clouds. The striped pattern in the southern hemisphere (latitudes >40S) is mainly associated with high viewing zenith angles in conjunction with high solar zenith angles that occur on one side of the swath.

Figure 11 similarly shows differences between CERES and OMI TOA SWF over ocean derived using f_c and OCP from the OMI O2-O2 product in place of the OMI RRS product. Because there are slight differences in the two cloud products, we retrained the network with

OMI O2-O2 cloud parameters to be consistent. The use of the O2-O2 f_c and OCP improves the accuracy of the estimated TOA SWF. The regions of improvement include the west coasts of South America and southern Africa and some parts of Indian Ocean. The O2-O2 cloud product, which uses visible wavelengths, is less affected by absorbing aerosol; this may explain the improvement in these areas where absorbing aerosol, especially over clouds, is common. However, negative biases remain over large regions off the west coast of Africa.

Figure 12a shows a time series of daily global mean values of TOA SWF over ocean from OMI and CERES for 2007. Both instruments show almost identical daily variations with differences within ±1%. Figure 12b, c provides monthly averaged (July 2007) CERES and OMI zonal and meridional means of TOA SWF. The OMI-derived TOA SWF is able to well reproduce the variability shown in the CERES data.

4.4 Spatial Distribution of TOA SWFs over Land

We developed a land NN model that utilizes most of the input parameters from our ocean NN (using OMI RRS cloud parameters). For surface characterization, we use a monthly climatology of surface broad-band albedo in place of the chlorophyll concentration and surface wind speed. The albedo product is derived using a combination of CERES and MODIS observations at 1 degree spatial resolution (Rutan et al., 2009).

Figure 13 shows results from the OMI-derived CERES-trained NN that produces TOA SWF over land. Statistical comparison with CERES over land provides results similar to those over ocean. The NN performs well over Asia and parts of Europe and the Americas. The OMI-based NN tends to underestimate TOA SWF over the high albedo desert areas of Northern Africa, Australia, and also over some regions of South America. Note large differences that occur in coastal regions may be due to imperfect collocations.

5 Summary and Conclusions

We have developed a neural network approach to estimate TOA SWF based primarily on UV measurements using the Aura OMI with Aqua CERES data used for training. One year of data from OMI and CERES has been used to train/validate/analyze several separate neural networks for different conditions, which together provide estimation of TOA SWF under all-sky conditions. The most important input parameters are effective cloud fraction and sun-satellite geometry. Total column ozone and cloud optical centroid pressure from OMI, as well as surface-related parameters, provide secondary positive impacts.

Independent validation at different spatial and temporal scales shows that the OMI NN-based approach reproduces CERES-derived TOA SWF with high fidelity. Correlation coefficients for all comparison are > 0.95, and slopes are close to unity. A high percentage of OMI-estimated monthly mean TOA SWF at 0.5^{o} spatial resolution over global oceans (97%) falls within 15% of CERES. The global mean bias in pixel level data of about -1.4 Wm^{-2} over oceans with respect to CERES is likely due in part to errors in OMI cloud parameters that occur in the presence of absorbing aerosols.

We plan to apply our derived neural networks to long-term well-calibrated UV measurements from TOMS. The TOMS series provides a long-term data record dating back to late 1978 (about half a decade before the first ERBE launch) with a few small gaps between that time and the first CERES launch. We should be able to apply NN models derived with CERES/OMI to TOMS, provided that all of the input parameters are available and compatible. In place of actual cloud OCPs that are available from OMI, but not from TOMS, we could use a cloud OCP climatology that was developed from OMI data for use in the TOMS total ozone algorithm. The lower spatial resolution of TOMS is not expected to present any difficulties. This approach can also be extended to the future geostationary missions such as TEMPO, GEMS and Sentinel 4.

Acknowledgements

This material is based upon work supported by the National Aeronautics and Space Administration issued through the Science Mission Directorate for the Aura Science Team managed by Kenneth Jucks and Richard Eckman. We thank the CERES, OMI, MODIS, and GEOS-DAS data processing teams for providing the data used for this study. We would also like to thanks Norman Loeb and Arlindo da Silva for useful discussion and comments during the preparation of manuscript.

References

Acarreta, J. R., De Haan, J. F., and Stammes, P.: Cloud pressure retrieval using the O_2-O_2 absorption band at 477 nm, J. Geophys. Res., 109, D05204, doi:10.1029/2003JD003915, 2004.

Barkstrom, B. R. and Smith, G. L.: The Earth radiation budget experiment: Science and implementation, Rev. Geophys., 24, 379– 390, 1986.

Barkstrom, B. R.: The Earth radiation budget experiment (ERBE), Bull. Am. Meteorol. Soc., 65, 1110–1185, 1984.

Baum, B. A., Yang, P., Heymsfield, A. J., Bansemer, A., Merrelli, A., Schmitt, C., and Wang, C.: Ice cloud bulk single-scattering property models with the full phase matrix at wavelengths from 0.2 to 100 µm, J. Quant. Spectrosc. Radiat. Trans., 146, 123-139, doi:10.1016/j.jqsrt.2014.02.029, 2014.

Bellouin, B., Boucher, O., Haywood, J., and Reddy, M. S.: Global estimates of aerosol direct radiative forcing from satellite measurements, Nature, 438, 1138–1140, doi:10.1038/nature04348, 2005.

Bishop, M.: Neural networks for pattern recognition, Oxford University Press, Inc., New York, 1995.

Bloom, S., da Silva, A., and Dee, D.: Technical Report Series on Global Modeling and Data Assimilation, edited by: Suarez, M. J., Documentation and Validation of the Goddard Earth Observing System (GEOS) Data Assimilation System–Version 4, NASA GSFC NASA/TM—2005–104606, 26, available at: http://gmao.gsfc.nasa.gov/systems/geos4/Bloom.pdf, 2005.

Chevallier, F., Cheruy, F., Scott, N. A., and Chedin, A.: A neural network approach for a fast and accurate computation of a longwave radiative budget, J. Appl. Meteorol., 37, 1385–1397, 1998.

Deirmendjian, D.: Electromagnetic scattering on spherical polydispersions, Elsevir Sci., New York, 290pp, 1969.

Dines, W. H.: The heat balance of the atmosphere, Q. J. R. Meteorol. Soc., 43, 151–158, 1917.

Domenech, C., and Wehr, T.: Use of Artificial Neural Networks to Retrieve TOA SW Radiative Fluxes for the EarthCARE Mission, IEEE Trans. Geosci. Remote Sens., 49, 1839-1849, 2011.

Atmos. Meas. Tech. Discuss., doi:10.5194/amt-2015-409, 2016
Manuscript under review for journal Atmos. Meas. Tech.
Published: 1 February 2016

Atmospheric Measurement Techniques
Discussions
Open Access

Gardner, M. W., and Dorling, S. R.: Artificial neural networks: A review of applications in the atmospheric sciences, Atmos. Environ., 32, 2627–2636, doi:10.1016/S1352-2310(97)00447-0, 1998.

Gupta, P., and Chirstophe, S. A.: Particulate matter air quality assessment using integrated surface, satellite, and meteorological products: 2. A neural network approach, J. Geophys. Res.,114, D20205, doi:10.1029/2008JD011497, 2009.

Harrison, E. F., Minnis, P., Barkstrom, B. R., Ramanathan, V., Cess, R. D., and Gibson, G. G.: Seasonal variation of cloud radiative forcing derived from the Earth Radiation Budget Experiment, J. Geophys. Res., 95, 18687–18703, 1990.

Hartmann, D. L., Ramanathan, V., Berroir, A., and Hunt, G. E.: Earth radiation budget data and climate research, Rev. Geophys., 24, 439–468, 1986.

Hatzianastassiou, N., Fotiadi, A., Matsoukas, Ch., Pavlakis, K., Drakakis, E., Hatzidimitriou, D., and Vardavas, I.: Long-term global distribution of earth's shortwave radiation budget at the top of atmosphere, Atmos. Chem. Phys., 4, 1217-1235, doi:10.5194/acp-4-1217-2004, 2004.

Hertz, J. A., Krogh, A. S., and Palmer, A.: Introduction to the Theory of Neural Computation, Addison-Wesley, Redwood City, Calif., 1991.

Hu, Y., Zhang, H., Wielicki, B., and Stackhouse, P.: A neural network MODIS-CERES narrowband to broadband conversion, IEEE Geoscience and Remote Sensing Symposium, 3227–32296, 2002.

Jiang, B., Zhang, Y., Liang, S., Zhang, X., and Xiou, Z.: Surface daytime net radiation estimate using artificial neural networks, Remote Sens., 6, 11031-11050, doi:10.3390/rs61111031, 2014.

Joiner, J. and Vasilkov, A. P.: First results from the OMI Rotational Raman Scattering Cloud Pressure Algorithm, IEEE Trans. Geosci. Remote Sens., 44, 1272–1282, 2006.

Joiner, J., and Bhartia, P. K.: The determination of cloud pressures from rotational-Raman scattering in satellite backscatter ultraviolet measurements, J. Geophys. Res., 100, 23,019-23,026, 1995.

Joiner, J., Schoeberl, M. R., Vasilkov, A. P., Oreopoulos, L., Platnick, S., Livesey, N. J., and Levelt, P. F.: Accurate satellite-derived estimates of the tropospheric ozone impact on the global radiation budget, Atmos. Chem. Phys., 9, 4447-4465, doi:10.5194/acp-9-4447-2009, 2009.

Joiner, J., Vasilkov, A. P., Flittner, D. E., Gleason, J. F., and Bhartia, P. K.: Retrieval of cloud chlorophyll content using Raman scattering in GOME spectra, J. Geophys. Res., 109, D01109, doi:10.1029/2003JD003698, 2004.

Joiner, J., Vasilkov, A. P., Gupta, P., Bhartia, P. K., Veefkind, P., Sneep, M., de Haan, J., Polonsky, I., and Spurr, R.: Fast simulators for satellite cloud optical centroid pressure retrievals; evaluation of OMI cloud retrievals, Atmos. Meas. Tech., 5, 529-545, doi:10.5194/amt-5-529-2012, 2012.

Krasnopolsky, V. M., Fox-Rabinovitz, and Belochitski, A. A.: Decadal climate simulations using accurate and fast neural network emulation of full, longwave and shortwave, radiation, Month. Weath. Rev., 136, 3683-3695, 2008.

Krasnopolsky, V. M., Fox-Rabinovitz, M. S., Hou, Y. T., Lord, S. J., Belochitski, A. A.: Accurate and fast neural network emulations of model radiation for the NCEP coupled climate forecast system: climate simulations and seasonal predictions, Month. Weath. Rev., 138, 1822-1842, 2010.

Kroon, M., Veefkind, J. P., Sneep, M., McPeters, R. D., Bhartia, P. K., and Levelt, P. F.: Comparing OMI-TOMS and OMIDOAS total ozone column data, J. Geophys. Res., 113, D16S28, doi:10.1029/2007JD008798, 2008.

Lee, J., Weger, R. C., Sengupta, S. K., and Welch, R. M.: A neural network approach to cloud classification, IEEE Trans. Geosci. Remote Sens., 28, 846 -85, 1990.

Levelt, P. F., van den Oord, G. H. J., Dobber, M. R., Mälkki, A., Visser, H., de Vries, J., Stammes, P., Lundell, J. O. V., and Saari, H.: The Ozone Monitoring Instrument, IEEE Trans. Geosci. Remote Sens., 44, 1093–1101, 2006.

Loeb, N. G., Manalo-Smith, N., Kato, S., Miller, W. F., Gupta, S. K., Minnis, P., and Wielicki, B. A.: Angular distribution models for top-of-atmosphere radiative flux estimation from the Clouds and the Earth's Radiant Energy System instrument on the Tropical Rainfall Measuring Mission Satellite, Part I: Methodology, J. Appl. Meteorol., 42, 240–265, 2003.

Loeb, N.G., and Manalo-Smith, N.: Top-of-Atmosphere direct radiative effect of aerosols over global oceans from merged CERES and MODIS observations, J. Climate, 18, 3506–3526, 2005.

Loeb, N. G., Kato, S., Loukachine, K., and Manalo-Smith, N.: Angular distribution models for top-of-atmosphere radiative flux estimation from the Clouds and the Earth's Radiant Energy System instrument on the Terra Satellite. Part I: Methodology, J. Atmos. Ocean. Tech., 22, 338–351, doi:10.1175/JTECH1712.1, 2005.

Loeb, N. G., Kato, S., Loukachine, K., Manalo-Smith, N., and Doelling, D. R.: Angular distribution models for top-of-atmosphere radiative flux estimation from the Clouds and the Earth's Radiant Energy System instrument on the Terra satellite. Part II: Validation, J. Atmos. Ocean. Tech., 24, 564–584, doi:10.1175/JTECH1983.1, 2007.

Loeb, N. G., Kato, S., Su, W., Wong, T., Rose, F. G., Doelling, D. R., Norris, J. R., and Huang, X.: Advances in understanding top-of-atmosphere radiation variability from satellite observations, Surv. Geophys., 33, 359–385, doi:10.1007/s10712-012-9175-1, 2012.

Loukachine, K., and Loeb, N. G.: Application of an artificial neural network simulation for top-of-atmosphere radiative flux estimation from CERES, J. Atmos. Oceanic Technol., 20, 1749–1757, 2003.

Loukachine, K., and Loeb, N. G.: Top-of-atmosphere flux retrievals from CERES using artificial neural networks, J. Remote Sens. Environ., 93, 381–390, 2004.

McPeters, R. D., Kroon, M., Labow, G. J., Brinksma, E., Balis, D., Petropavlovskikh, I., Veefkind, J. P., Bhartia, P. K., and Levelt, P. F.: Validation of the Aura Ozone Monitoring Instrument Total Column Ozone Product, J. Geophys. Res., 113, D15S14, doi:10.1029/2007JD008802, 2008

Oreopoulos, L., Platnick, S., Hong, G., Yang, P., and Cahalan, R. F.: The shortwave radiative forcing bias of liquid and ice clouds from MODIS observations, Atmos. Chem. Phys., 9, 5865-5875, doi:10.5194/acp-9-5865-2009, 2009.

Patadia, F., Christopher, S. A., and Zhang, J.: Development of empirical angular distribution models for smoke aerosols: Methods, J. Geophys. Res., 116, 1984–2012, 2011.

Patadia, F., Gupta, P., and Christopher, S. A.: First observational estimates of global clear sky shortwave aerosol direct radiative effect over land, Geophys. Res. Lett., 35, L04810, doi:10.1029/2007GL032314, 2008.

Ramanathan, V., Cess, R. D., Harrison, E. F., Minnis, P., Barkstrom, B. R., Ahmad, E., and Hartmann, D.: Cloud radiative forcing and climate: Results from the Earth Radiation Budget Experiment, Science, 243, 57–63, 1989b.

Rutan, D., Rose, F., Roman, M., Manalo-Smith, N., Schaaf, C., and Charlock, T.: Development and assessment of broadband surface albedo from Clouds and the Earth's Radiant Energy System Clouds and Radiation Swath data product, J. Geophys. Res., 114, D08125, doi:10.1029/2008JD010669, 2009.

Stammes, P., Sneep, M., de Haan, J. F., Veefkind, J. P., Wang, P., and Levelt, P. F.: Effective cloud fractions from the Ozone Monitoring Instrument: theoretical framework and validation, J. Geophys. Res., 113, D16S38, doi:10.1029/2007JD008820, 2008.

Takenaka, H., Nakajima, T. Y., Higurashi, A., Higuchi, A., Takamura, T., Pinker, R. T., and Nakajima, T.: Estimation of solar radiation using a neural network based on radiative transfer, J. Geophys. Res., 116, D08215, doi: 10.1029/2009JD013337.

van de Hulst, H. C., Irvine, W. M.: General report on radiation transfer in planets: Scattering in model planetary atmospheres, Mem. Soc. R. Sci. Liege, 7, 78-98, 1963.

Vasilkov, A. P., Joiner, J., Spurr, R., Bhartia, P. K., Levelt, P. F., and Stephens, G.: Evaluation of the OMI cloud pressures derived from rotational Raman scattering by comparisons with other satellite data and radiative transfer simulations, J. Geophys. Res., 113, D15S19, doi:10.1029/2007JD008689, 2008.

Vázquez-Navarro, M., Mayer, B., and Mannstein, H.: A fast method for the retrieval of integrated longwave and shortwave top-of-atmosphere upwelling irradiances from MSG/SEVIRI (RRUMS), Atmos. Meas. Tech., 6, 2627-2640, doi:10.5194/amt-6-2627-2013, 2013.

Atmos. Meas. Tech. Discuss., doi:10.5194/amt-2015-409, 2016
Manuscript under review for journal Atmos. Meas. Tech.
Published: 1 February 2016

Veefkind, J. P., de Haan, J. F., Brinksma, E. J., Kroon, M., and Levelt, P. F.: Total ozone from the ozone monitoring instrument (OMI) using the DOAS technique, IEEE Trans. Geosci. Remote Sens., 44, 1239–1244, 2006.

Wielicki, B. A., Harrison, E. F., Cess, R. D., King, M. D., and Randall, D. A.: Mission to planet Earth: Role of clouds and radiation in climate, Bull. Amer. Meteorol. Soc., 76, 2125–2153, 1995.

Yu, H., Kaufman, Y. J., Chin, M., Feingold, G., Remer, L. A., Anderson, T. L., Balkanski, Y., Bellouin, N., Boucher, O., Christopher, S., DeCola, P., Kahn, R., Koch, D., Loeb, N., Reddy, M. S., Schulz, M., Takemura, T., and Zhou, M.: A review of measurement-based assessments of the aerosol direct radiative effect and forcing, Atmos. Chem. Phys., 6, 613-666, doi:10.5194/acp-6-613-2006, 2006.

Zhang, J., Christopher, S. A., Remer, L. A., and Kaufman, Y. J.: Shortwave aerosol radiative forcing over cloud-free oceans from Terra. I: Angular models for aerosols, J. Geophys. Res., 110, D10S23, doi:10.1029/2004JD005008, 2005a.

Zhang, J., Christopher, S. A., Remer, L. A., and Kaufman, Y. J.: Shortwave aerosol radiative forcing over cloud-free oceans from Terra. II: Seasonal and global distributions, J. Geophys. Res., 110, D10S24, doi:10.1029/2004JD005009, 2005b.

Atmos. Meas. Tech. Discuss., doi:10.5194/amt-2015-409, 2016
Manuscript under review for journal Atmos. Meas. Tech.
Published: 1 February 2016

Atmospheric Measurement Techniques Discussions

Table 1. Statistical analysis of the input parameter selection exercise. The correlation coefficient (R), Slope (slope), Bias, and standard deviation of OMI-CERES TOA SW flux for eight different NN models are presented. These numbers correspond to daily inter-comparison between OMI and CERES TOA SW flux. Data from January 2007 is used for this exercise.

Model	**Parameters**	**R**	**Slope**	**Bias**	**STD ($W\ m^{-2}$)**
a	f_{c_mod}	0.971	0.941	0.051	37.1
b	f_{c_mod},, VZA, RAA	0.979	0.959	0.000	31.4
c	LER, SZA, VZA, RAA	0.979	0.959	-0.030	31.1
d	f_{c_mod},, VZA, RAA, O3	0.980	0.960	-0.009	30.9
e	f_{c_mod},, VZA, RAA, OCP	0.981	0.962	-0.004	30.0
f	f_{c_mod}, VZA, RAA, O3, OCP	0.981	0.963	0.002	29.9
g	f_{c_mod}, VZA, RAA, O3, OCP, PW, Wind	0.982	0.964	0.002	29.2
h	f_{c_mod}, VZA, RAA, O3, OCP, PW, Wind, Chl, LER	0.983	0.967	-0.010	28.3

Atmos. Meas. Tech. Discuss., doi:10.5194/amt-2015-409, 2016
Manuscript under review for journal Atmos. Meas. Tech.
Published: 1 February 2016

Atmospheric Measurement Techniques Discussions
Open Access

Table 2. Statistical parameters corresponding daily and monthly inter-comparisons of pixel and grid levels TOA SW flux data from CERES and OMI.

	N	**R**	**M**	**I**	**BIAS**	**STD**	**EE5%**	**EE10%**	**EE15%**
Pixel	8109323	0.96	0.96	10.5	-1.4	47.7	30	53	69
					Daily				
0.5°	1512726	0.97	0.96	11.2	0.94	34.4	37	62	77
1°	529679	0.98	0.96	11.2	1.0	27.9	43	69	83
2°	168181	0.98	0.96	11.0	0.33	23.7	50	76	87
5°	35454	0.99	0.96	9.2	-1.8	20.3	60	84	92
10°	10834	0.99	0.97	7.0	-0.0	14.6	69	90	97
					Monthly				
0.5°	108620	0.99	0.98	6.1	1.5	12.9	74	93	97
1°	28849	0.99	0.98	6.9	1.2	11.4	79	94	98
2°	7642	0.99	0.96	9.8	0.25	6.6	94	99	100
5°	1325	0.99	0.96	9.9	-1.8	7.0	95	99	100

Note: N – Number of pairs, R- correlation coefficient, M- Slope, I- Intercept, Bias – mean of (OMI-CERES in Wm^{-2}), STD- standard deviation of (OMI-CERES) in Wm^{-2}, EE –Error Envelope for 5%,10%,15% errors. All flux values have units of Wm^{-2}

Atmos. Meas. Tech. Discuss., doi:10.5194/amt-2015-409, 2016
Manuscript under review for journal Atmos. Meas. Tech.
Published: 1 February 2016

Atmospheric Measurement Techniques
Discussions

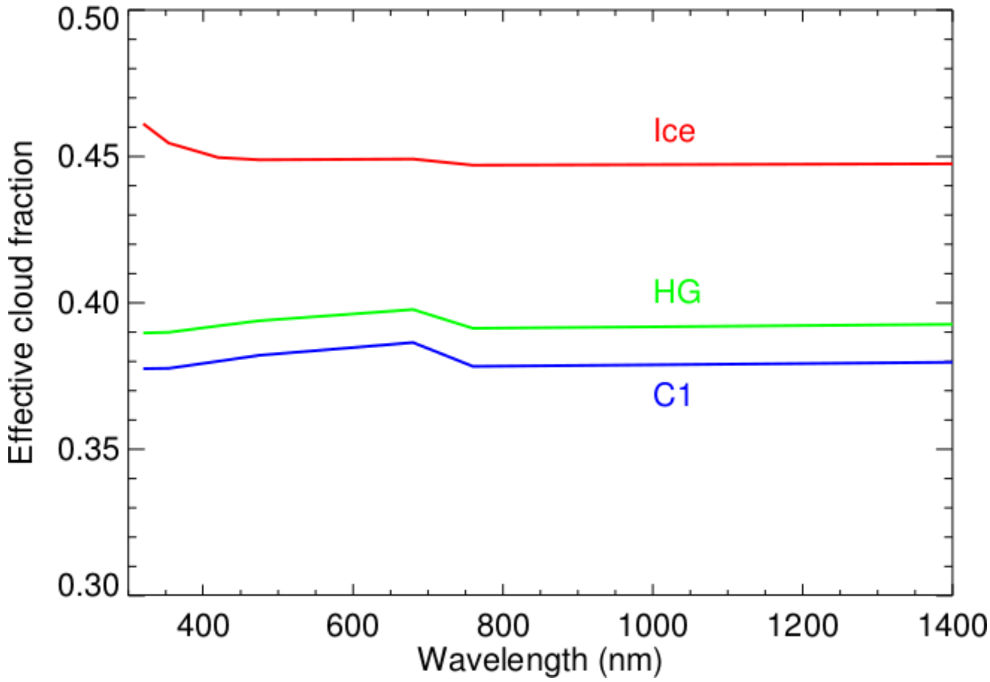

Figure 1. The spectral dependence of the effective cloud fraction for land, f_g =0.5, SZA = 45^0, observation at nadir. Red line: ice phase function; Green line: the Heneye-Greenstein function, Blue line: C1 model.

Atmos. Meas. Tech. Discuss., doi:10.5194/amt-2015-409, 2016
Manuscript under review for journal Atmos. Meas. Tech.
Published: 1 February 2016

Atmospheric Measurement Techniques
Discussions
Open Access

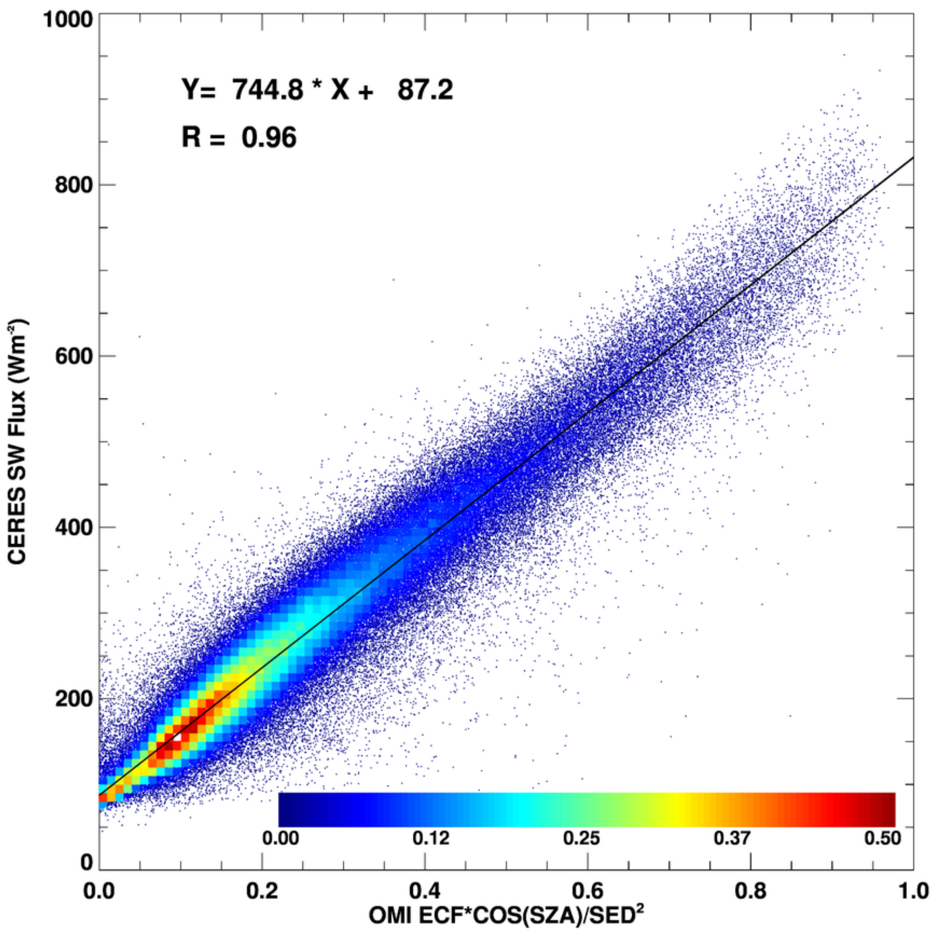

Figure 2. 2D histogram of effective cloud fraction (ECF or f_c) normalized (i.e. f_{c_mod}) with respect to incoming solar irradiance and CERES TOA shortwave (SW) flux over ocean.

Atmos. Meas. Tech. Discuss., doi:10.5194/amt-2015-409, 2016
Manuscript under review for journal Atmos. Meas. Tech.
Published: 1 February 2016

Atmospheric Measurement Techniques Discussions

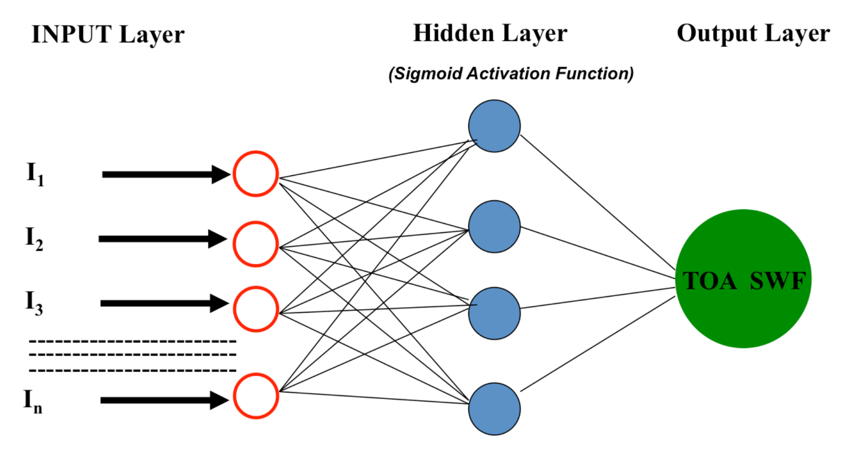

Neural Network Model	Input Parameters
NNM – 1 [f_c<1.0]	f_{c_mod}, VZA, RAA, OCP, O3, WINDS, PW, CHL, LER
NNM – 2 [f_c≥1.0]	SZA, VZA, RAA, OCP, LER, O3, PW

Figure 3. A schematic of the neural network model used for estimation of TOA SW flux with OMI UV measurements. The table in the bottom lists all the input parameters corresponding to two NN models used.

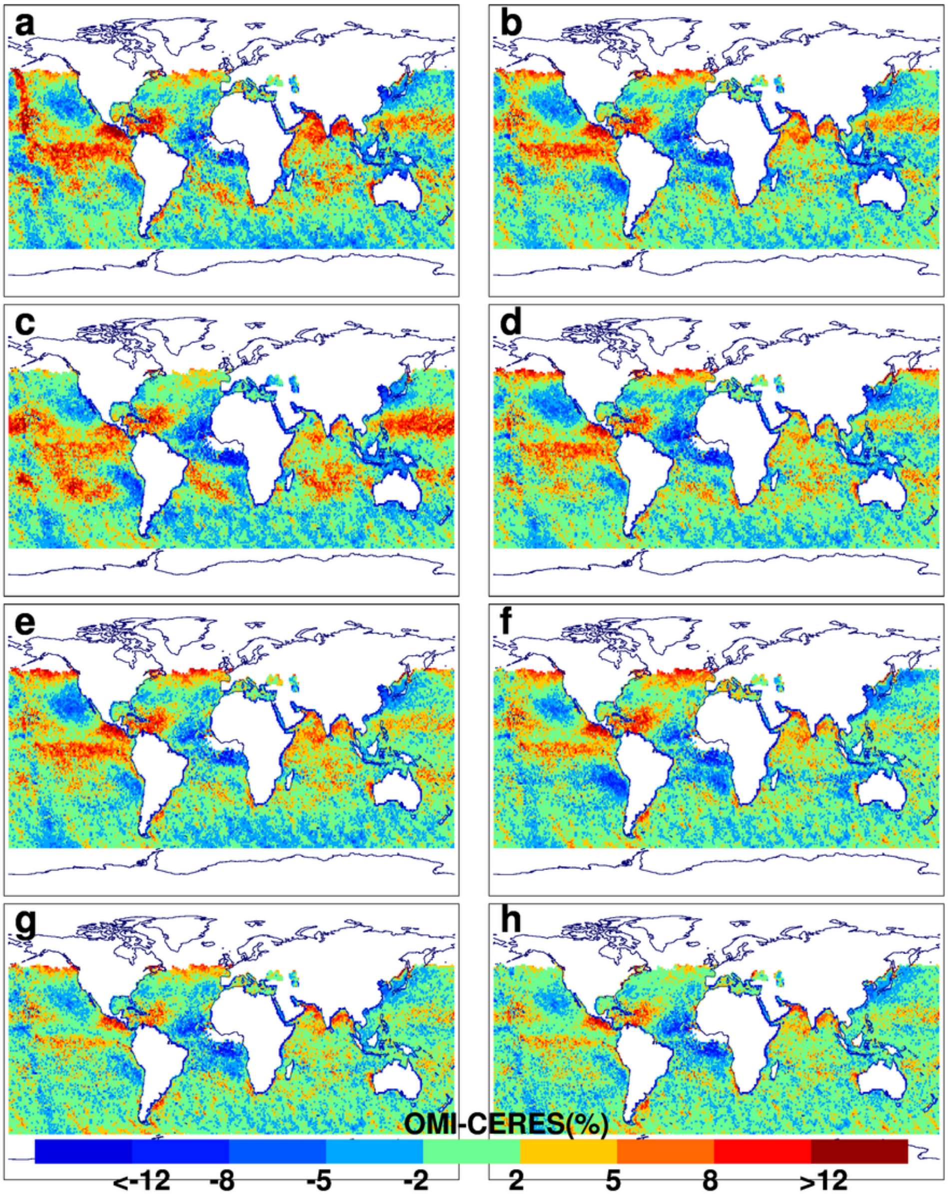

Figure 4. Monthly mean (January 2007) maps of OMI minus CERES TOA SW flux (%) for eight different NN models. The letters on the map corresponds to model number in the table 1.

Atmos. Meas. Tech. Discuss., doi:10.5194/amt-2015-409, 2016
Manuscript under review for journal Atmos. Meas. Tech.
Published: 1 February 2016

Atmospheric Measurement Techniques Discussions

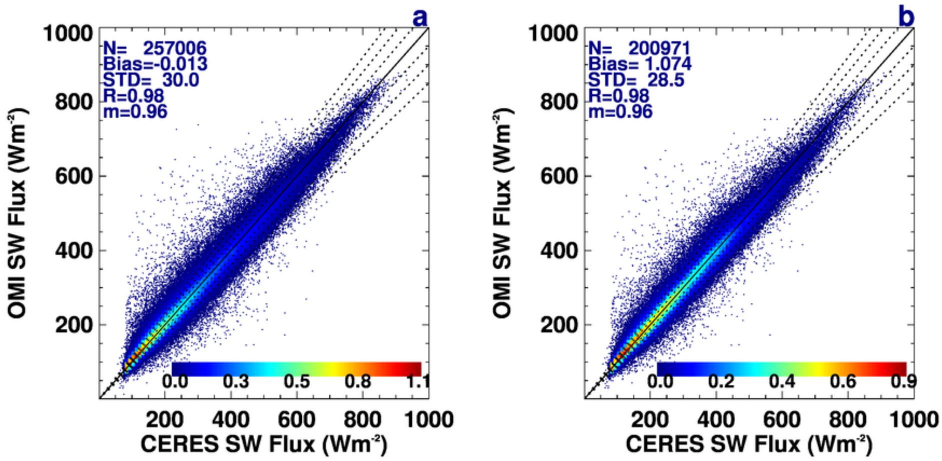

Figure 5. 2D histograms of daily CERES and OMI SW flux for month of January 2007. a) NN is trained and applied to January 2007 b) NN is trained on January 2007 and applied to January 2006.

Atmos. Meas. Tech. Discuss., doi:10.5194/amt-2015-409, 2016
Manuscript under review for journal Atmos. Meas. Tech.
Published: 1 February 2016

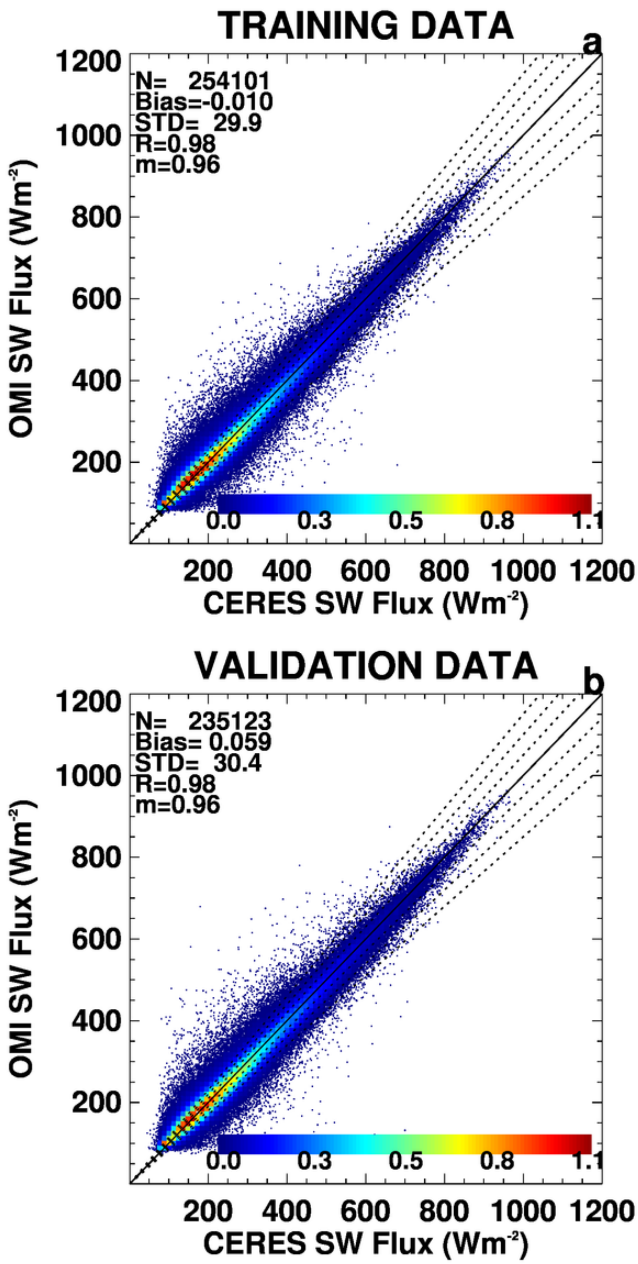

Figure 6. Similar to Fig. 5 but showing training (top) and validation (bottom) results from two NN models (input parameters listed in Figure 3, model h for f_c<1 and as in Figure 3 for f_c>1) as final selected models for estimation of TOA SW Flux.

Atmos. Meas. Tech. Discuss., doi:10.5194/amt-2015-409, 2016
Manuscript under review for journal Atmos. Meas. Tech.
Published: 1 February 2016

Atmospheric Measurement Techniques Discussions

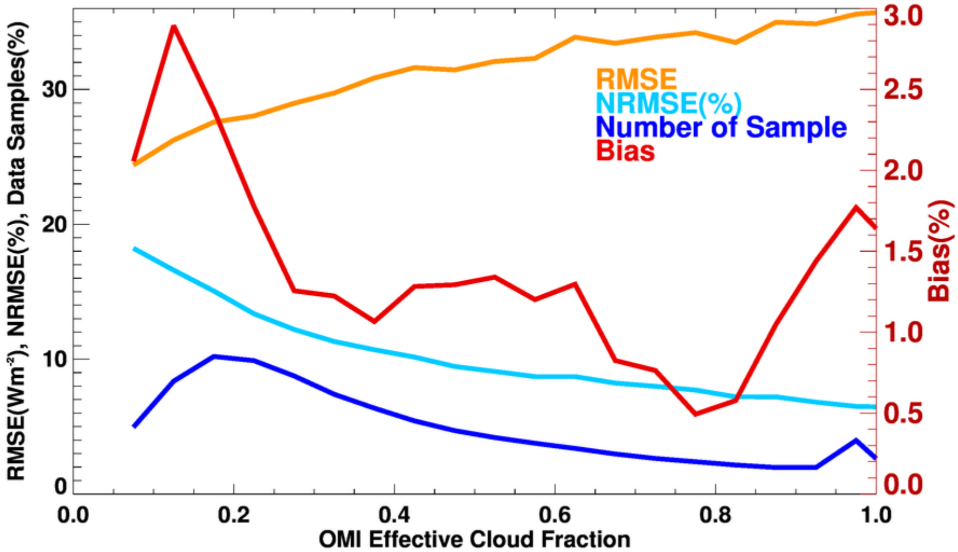

Figure 7. Root mean squared errors (RMSE), normalized RMSE (NRMSE in %), data samples (%), and bias (%) in training and validation data sets as a function of effective cloud fraction for the data presented in Figure 4.

Atmos. Meas. Tech. Discuss., doi:10.5194/amt-2015-409, 2016
Manuscript under review for journal Atmos. Meas. Tech.
Published: 1 February 2016

Atmospheric Measurement Techniques Discussions

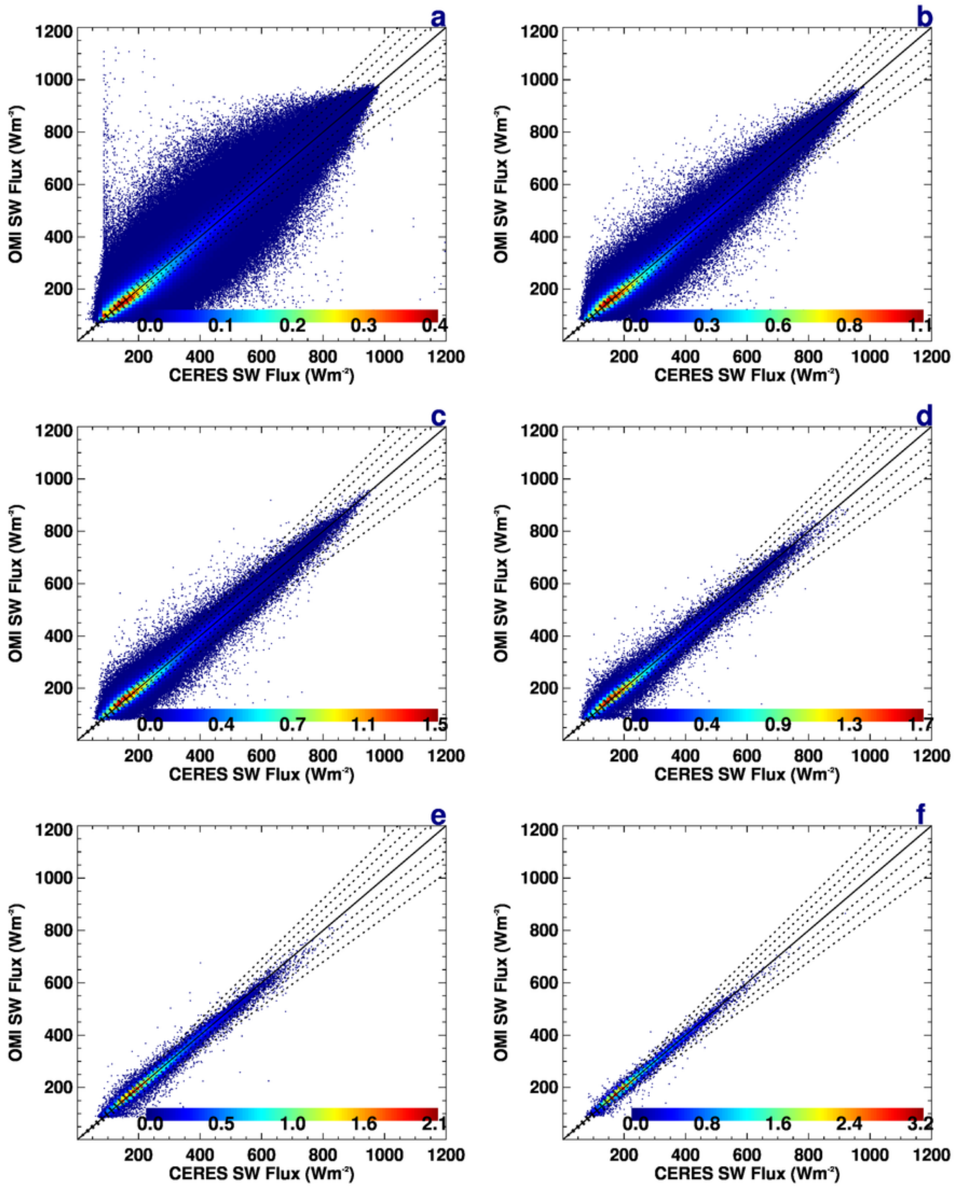

Figure 8. 2D histograms of the daily OMI and CERES TOA SW Flux averaged over different spatial grid sizes for the month of July 2007. a) at OMI's native pixel resolution b) 0.5x0.5 degree c) 1x1 degree d) 2x2 degree e) 5x5 degree and f) 10x10 degree. The corresponding statistical parameters are listed in table 2.

Atmos. Meas. Tech. Discuss., doi:10.5194/amt-2015-409, 2016
Manuscript under review for journal Atmos. Meas. Tech.
Published: 1 February 2016

Atmospheric Measurement Techniques
Discussions

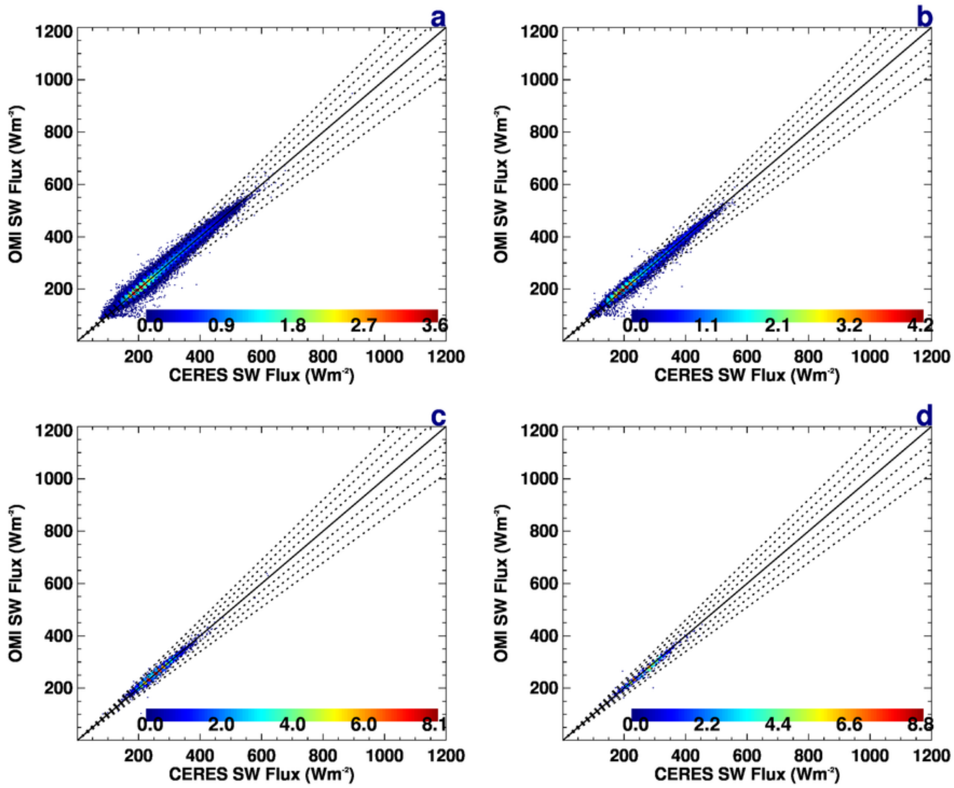

Figure 9. Similar to Fig. 8 but for monthly mean data (July 2007) OMI and CERES TOA SW flux averaged over different spatial grid sizes. a) 0.5x0.5 degree b) 1x1 degree c) 2x2 degree d) 5x5 degree. The corresponding statistical parameters are listed in table 2.

Atmos. Meas. Tech. Discuss., doi:10.5194/amt-2015-409, 2016
Manuscript under review for journal Atmos. Meas. Tech.
Published: 1 February 2016

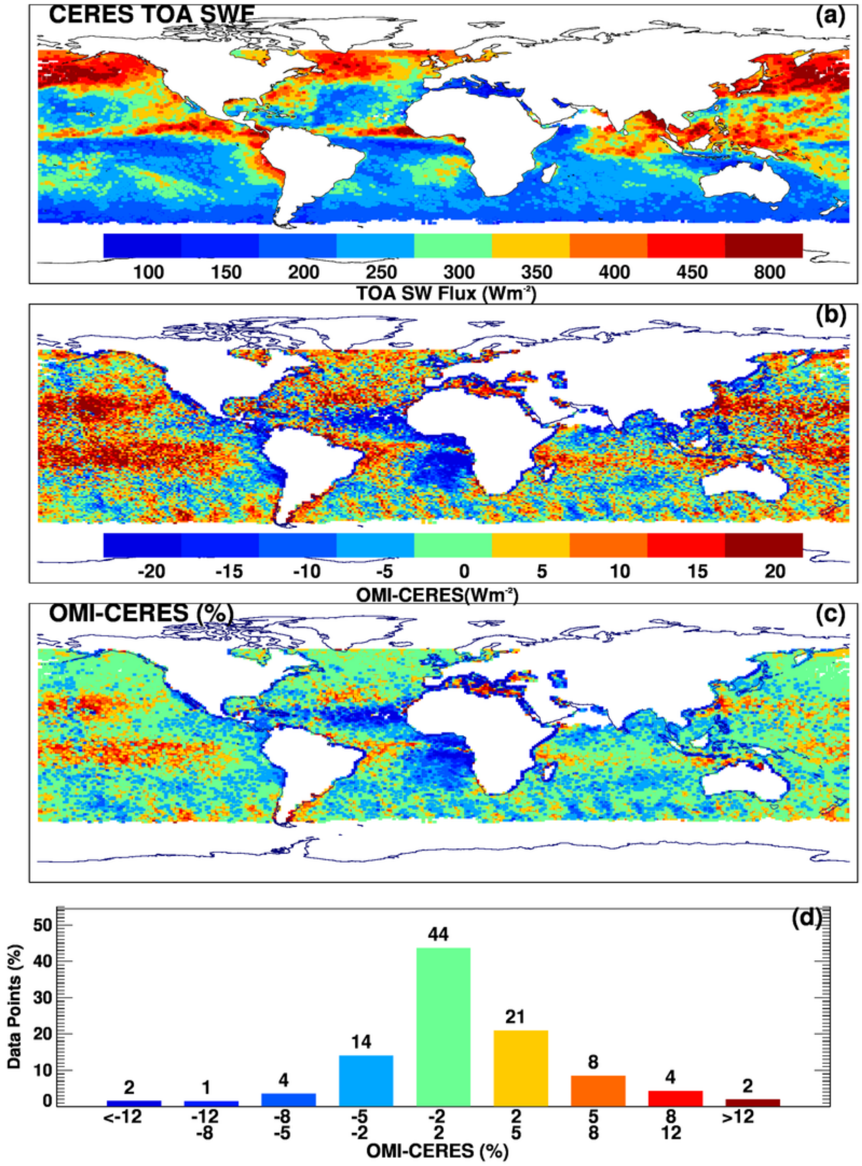

Figure 10. a) Monthly mean (July 2007) spatial distribution of TOA SW flux from CERES; b) OMI-CERES (in Wm^{-2}); c) OMI-CERES (%); d) histogram of OMI-CERES % . The colors in (c) correspond to histogram colors in (d).

Atmos. Meas. Tech. Discuss., doi:10.5194/amt-2015-409, 2016
Manuscript under review for journal Atmos. Meas. Tech.
Published: 1 February 2016

Atmospheric Measurement Techniques
Open Access
Discussions

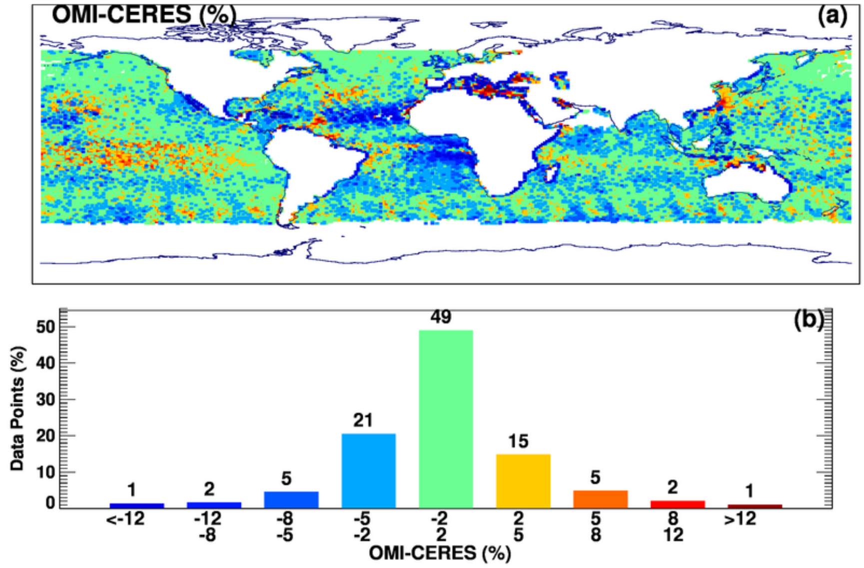

Figure 11. Similar to Fig. 10c and d, but with a NN trained using data from the OMI cloud O_2-O_2 product.

Atmos. Meas. Tech. Discuss., doi:10.5194/amt-2015-409, 2016
Manuscript under review for journal Atmos. Meas. Tech.
Published: 1 February 2016

Atmospheric Measurement Techniques
Open Access
Discussions

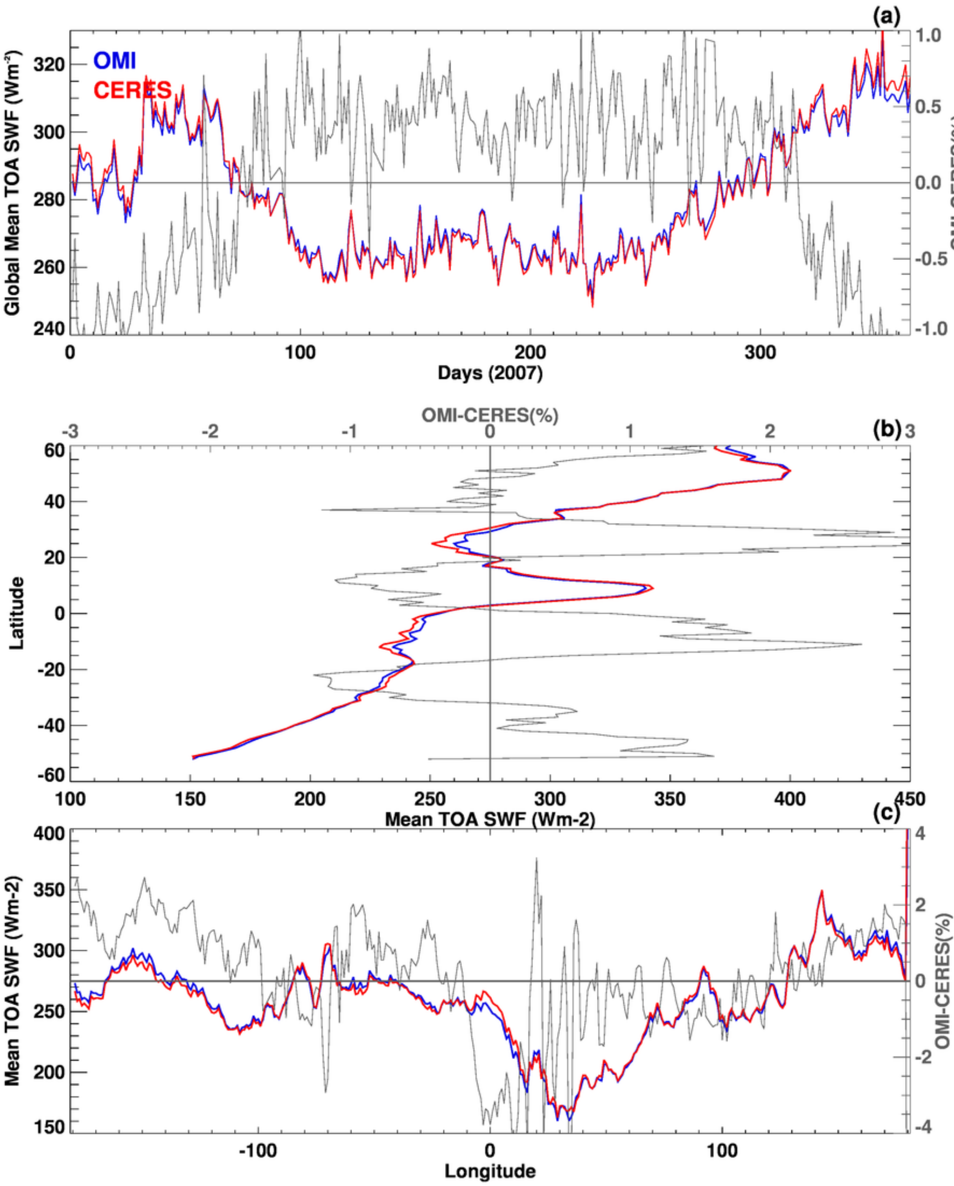

Figure 12. a) The daily global mean time series of TOA SW fluxes from NN and CERES and also shows OMI-CERES (%) on secondary y-axis; b) Mean TOA SW flux from CERES and OMI averaged along each latitude belt, and also shown OMI-CERES (%) on secondary x-axis. c) same as b but along longitude belts. The data used in b and c are from July 2007.

Atmos. Meas. Tech. Discuss., doi:10.5194/amt-2015-409, 2016
Manuscript under review for journal Atmos. Meas. Tech.
Published: 1 February 2016

Atmospheric Measurement Techniques
Open Access
Discussions

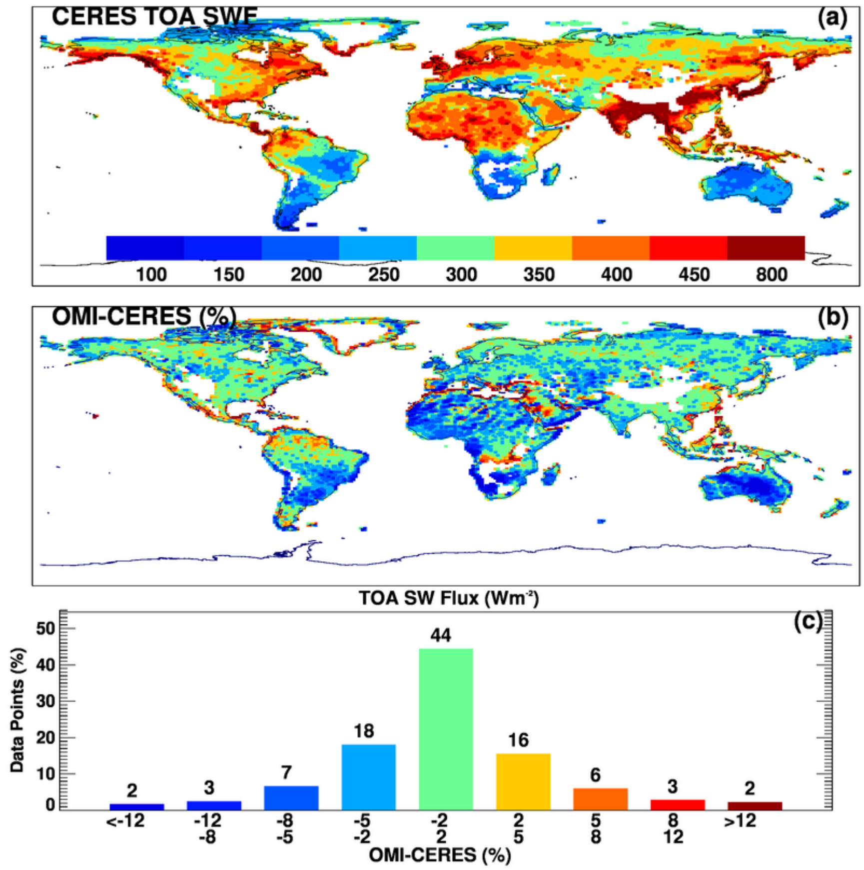

Figure 13. Similar to Fig. 10 (a, c, d) except over land.